Title

High-pressure study of dravite tourmaline: Insights into the accommodating nature of the tourmaline structure

Journal

American Mineralogist, 103(10)

ISSN

0003-004X

Authors

O'Bannon, Earl
Beavers, Christine M
Kunz, Martin
et al.

Publication Date

2018-10-01

DOI

10.2138/am-2018-6486

High-pressure study of dravite tourmaline: Insights into the accommodating nature of the tourmaline structure

Earl O'Bannon III,[1*] Christine M. Beavers[2,3], Martin Kunz[3], and Quentin Williams[2]

[1]Physics Division, Lawrence Livermore National Laboratory, Livermore, California 94550, USA

[2]Department of Earth and Planetary Sciences, University of California Santa Cruz, Santa Cruz, California 95064, USA

[3]Advanced Light Source, Lawrence Berkeley National Laboratory, Berkeley, California, 94720, USA

*Corresponding Author

Abstract

The high-pressure behavior of dravite tourmaline [$Na(Mg_3)Al_6(Si_6O_{18})(BO_3)_3(OH)_3(OH)$] has been studied using luminescence spectroscopy and synchrotron based single-crystal diffraction up to ~65 and ~23.6 GPa, respectively. Two emission bands associated with Cr^{3+}/V^{2+} substitution are constant in energy up to ~9.0 GPa, and shift to longer wavelength at higher pressures, suggesting that a change in compressional mechanism could occur at this pressure. However, single-crystal diffraction data do not show evidence of any structural changes, nor any resolvable changes in the deformation mechanism at ~9.0 GPa. Near 15 GPa, a splitting of one of the emission bands is observed, suggesting that a phase transition occurs at this pressure and that two unique octahedral sites are present in the high-pressure phase. Hysteresis is not observed on decompression, which indicates that this is a second order transition, and the high-pressure structure appears to be metastable up to ~65 GPa. Single-crystal diffraction measurements show that a phase transition from rhombohedral *R*3*m* to rhombohedral *R*3 occurs at pressures near 15.4 GPa. The high-pressure phase is characterized

by a distorted Si_6O_{18} ring (e.g. the Si-Si-Si angles deviate from 120°), and the Si, Al, O6, O7, and O8 sites of the low-pressure phase split, implying that the high-pressure phase of tourmaline is a higher entropy phase. The large *X*-site exerts the primary control on compressibility, and the substitution of larger cations into this site will likely lower the pressure at which this transition occurs. Dravite tourmaline shows anisotropic compression with the *c*-axis being more compressible thant the *a*-axis. The pressure volume data up to ~15.4 GPa were fit with 2nd and 3rd order Birch-Murnaghan equations of state. We obtain a bulk modulus, K_0= 109.0(2.9) GPa, and a pressure derivative K_0' = 4.8(8) GPa, and with the pressure derivative set to 4, a bulk modulus of 112.2(9) GPa is derived.

Key Words: dravite; High-pressure; Single-crystal diffraction, luminescence, phase transitions

Introduction

Tourmaline is a supergroup of minerals that is chemically complex and is divided into different varieties based on chemical composition (Hawthorne and Henry 1999; Henry et al. 2011). This group of minerals is so complex and chemically variable that an entire subcommittee on tourmaline nomenclature exists. These minerals are categorized using the generalized tourmaline structural formula $XY_3Z_6(T_6O_{18})(BO_3)_3V_3W$ where *X* = Na, Ca, K; *Y* = Fe, Mg, Mn, Al, Li; *Z* = Al, Fe, Mg, Cr; *T* = Si, Al; *B*= B; *V* = (OH), O; and *W* = (OH), O, F (Hawthorne and Henry 1999; Henry et al. 2011). From a compositional perspective, most of the variability occurs in the *X*, *Y*, and *Z* sites; more information on the classification of tourmaline supergroup minerals can be found in Hawthorne and Henry (1999) and Henry et al. (2011). Tourmaline is also highly sought after as a gemstone due to its high hardness and wide range of colors.

Tourmaline typically crystallizes in the rhombohedral crystal system with *R*3*m* symmetry (Hawthorne and Henry 1999; Henry et al. 2011), although other crystal systems have been reported (Akizuri et al. 2001; Shtukenberg et al. 2007). It is typically considered a ring-silicate with six corner-shared TO_4 tetrahedral sites that form a hexagonal ring, a nine-fold *X*-site, two six-fold octahedral *Y*- and *Z*-sites, and a trigonal planar *B*-site (Figure 1). Although the T-sites are dominantly occupied by Si, B and Li substitution into them has been reported (Rosenberg and Foit 1979; Hughes et al. 2000). Interestingly, the first reported structure of tourmaline presented the Si_6O_{18} ring as ditrigonal in symmetry (Hamburger and Buerger 1948). However, it was later shown to be hexagonal in symmetry (Ito and Sadanaga 1951), and all subsequent studies agree that the Si_6O_{18} ring is hexagonal at ambient conditions.

Tourmaline is the most widespread borosilicate mineral in natural rocks and the dominant carrier of B in many rock types (Henry and Dutrow, 1996), and is found in subduction zone environments (Nakano and Nakamura 2001; Bebout and Nakamura 2003; Ota et al. 2008). B isotope systematics in tourmalines have been used to elucidate crust-mantle recycling processes in subduction zones (Nakano and Nakamura, 2001). Petrologic studies have shown that dravite tourmaline breaks down at ~7.0 GPa and ~900 °C (Werding and Schreyer 1996) and ~3-5 GPa and ~1000 °C (Krosse 1995) and that breakdown pressures and temperatures are dependent on its precise composition (Ota et al. 2008). The decomposition products associated with tourmaline breakdown are complex, but one decomposition product, phengite, is important from a deep Earth boron and water cycling perspective; phengite could transport B to depths >300 km (Domanik and Holloway 1996; Marschall et al. 2007). Higher pressure studies (e.g. > 7.0 GPa) on tourmaline are scarce, and only two studies appear to have been reported: Li

et al., (2004) and Xu et al., (2016). Li et al. (2004) conducted high-pressure powder diffraction experiments on schorl tourmaline [$Na(Fe_3)Al_6(Si_6O_{18})(BO_3)_3(OH)_3(OH)$] up to 27.8 GPa, with no phase transitions being reported. Xu et al. (2016) reported high-pressure and temperature powder diffraction experiments on uvite tourmaline [$Ca(Mg_3)MgAl_5(Si_6O_{18})(BO_3)_3(OH)_3(OH)$] up to ~18.4 GPa and 723 K and again, no phase transitions were observed. These powder diffraction studies provide insights into how the unit cell responds to compression, but they do not elucidate the positional changes of the individual atoms in the unit cell (Li et al. 2004; Xu et al. 2016).

This is in contrast to other ring-silicates such as cordierite [$(Mg, Fe)_2Al_3(AlSi_5O_{18})$] and beryl [$Be_3Al_2(Si_6O_{18})$] which each show extensive high-pressure polymorphism (Prencipe et al. 2011; Miletich et al. 2014; Scheidl et al. 2014; Finkelstein et al. 2015; O'Bannon and Williams 2016b). Both cordierite and beryl undergo high-pressure phase transitions that involve distortion of the Si_6O_{18} ring. The main structural difference between tourmaline and these other ring silicates is that tourmaline does not have open channels in its structure like cordierite and beryl. Thus, it is possible that the denser-packed configuration of the Si_6O_{18} rings in tourmaline produces a structure that is more stable under compression than open channel ring silicates like cordierite or beryl.

Tourmaline is also both pyroelectric and piezoelectric, and has been used in industrial applications such as pressure gauges and air and water purifiers (Frondel 1948; Lameiras et al. 2010). Growing synthetic tourmalines >1mm in diameter has not yet been achieved, and thus industrial applications require natural tourmalines (Shekhar Pandey and Schreuer 2012). Thus, despite its widespread use in industrial applications and as a geochemical probe, tourmaline's

high-pressure stability/polymorphism is poorly understood. Hence, our experiments are oriented towards understanding the trace element behavior and the bulk structural response of dravite tourmaline to compression by combining the results of luminescence and single-crystal diffraction studies to provide an integrated picture of structural changes in dravite tourmaline under compression.

Methods

2.1 Sample characterization

The natural light green gem quality tourmaline sample used in this study is from the Lengenbach Quarry, Switzerland. We characterized the sample with single-crystal X-ray diffraction, Raman, and luminescence spectroscopy, which all agree well with previous studies (Hawthorne et al. 1993; Gasharova et al. 1997; Gaft et al. 2005). Ambient pressure single-crystal X-ray measurements were conducted on Beamline 11.3.1 at the Advanced Light Source (ALS) at Lawrence Berkeley National Lab in Berkeley, CA. We modeled our tourmaline as an endmember dravite and our ambient structure refines with an R_1 of 1.85% when refined anisotropically and 2.99% when refined isotropically. Its crystal system, spacegroup and unit cell parameters are: rhombohedral *R*3*m*, *a*-axis 15.9370(6) Å, *c*-axis 7.1749(3) Å, and volume 1578.19(14) $Å^3$, respectively. For the ambient structure refinement, we fixed the O1-H1 and O3-H3 bond lengths to 0.958(8) and 0.972(2) Å, respectively. These bond lengths were determined from previous neutron diffraction results on tourmaline (Gatta et al. 2014). Trace element concentrations of dravite tourmaline were measured with a PhotonMachines Analyte 193H, which is a 193-nm ArF excimer laser system coupled with a ThermoScientific ElementXR single-collect or magnetic sector ICP-MS. The instrument was calibrated with a SRM 610 trace element glass from NIST,

and Al was used as the internal standard. The following trace elements were measured (in ppm): Cr 215 (±19), V 336 (±32), Li 18 (±4.0), Ti 474 (±53), Ca 2183 (±597), and K, Fe, and Mn are below detection limits. The Subcommittee on Tourmaline Nomenclature (STN) of the IMA Commission on New Minerals, Nomenclature and Classification recommends nomenclature of tourmaline supergroup minerals (Novak et al., 2009; Henry et al., 2011; Hawthorne and Dirlam, 2011). Using our single-crystal X-ray results combined with our trace element results, and following STN recommendations, we determined that this tourmaline is of the dravite variety. Dravite variety tourmaline has an ideal chemical formula of $[Na(Mg_3)Al_6(Si_6O_{18})(BO_3)_3(OH)_3(OH)]$. Hence, the structures were refined isotropically and modeled as endmember dravite tourmaline: this allowed direct comparisons of the results obtained at each pressure.

2.2 Luminescence spectroscopy

Luminescence spectra were collected from 650-800 nm (15380-12500 cm^{-1}) with a Horiba LabRAM HR Evolution Raman spectrometer with a spectrometer focal length of 800 mm. Spectra were collected to a pressure of ~65 GPa and on decompression at 300 K using an excitation wavelength of 532 nm. A symmetric type DAC with 200 µm type-Ia diamonds was used in all high-pressure luminescence experiments, and single crystals of the sample and at least two ruby spheres (Chervin et al. 2001) were loaded into the sample compartment. Either 4:1 methanol:ethanol mixtures or Ne was used as the pressure medium depending on the target pressure range of the experiment. An Olympus BXFM-ILHS microscope with a 50x long working distance objective was used to focus the laser beam onto the sample. An 1800 lines/mm grating with a corresponding spectral resolution of ~1 cm^{-1} (or, equivalently, ~0.05 nm)

was utilized. Combinations of Gaussian and Lorentzian functions were fit to the luminescence spectra with Horiba Labspec6 software.

2.3 High-pressure single crystal diffraction

High-pressure single-crystal measurements were carried out using a (DESY) BX90 (Kantor et al. 2012) type diamond anvil cell (DAC) equipped with type Ia 500 µm culet Boehler-Almax geometry diamond anvils with 85° angular access (Boehler and De Hantsetters 2004). Rhenium gaskets with a 300 µm hole were used to contain the samples. Gasket holes were cut using an Oxford Instruments laser mill at the Advanced Light Source (ALS), Berkeley, CA. Single crystals of dravite tourmaline and two ruby spheres were loaded into the sample compartment with neon as the pressure medium. The standard ruby fluorescence gauge was used to determine pressure (Mao et al. 1986). Neon was loaded using the gas loading apparatus at the ALS. Neon remains hydrostatic up to ~15.0 GPa and above that pressure, the pressure gradients remain small (Klotz et al. 2009).

High-pressure single-crystal X-ray diffraction measurements were conducted at Beamline 12.2.2 at the ALS. Measurements were taken at various pressures up to ~23.6 GPa at room temperature. The DAC was mounted on a Huber sample stage, and shutterless single-crystal diffraction data were collected on a Perkin Elmer amorphous silicon detector using synchrotron radiation monochromated by silicon(111) to a wavelength of 0.49594 Å (25 keV). Distance and wavelength calibrations were done using a NIST single crystal ruby diffraction standard. Phi scans were employed to measure across both diamonds with a 0.25° image width.

2.4 Data processing

Image masks, to avoid integrating signal from detector regions obscured by the DAC,

were created using the program ECLIPSE (Parsons 2010). The data were integrated using the program SAINT v8.34A. A multi-scan correction for absorption was applied using the program SADABS-2014/11. Structures were solved by dual space methods (SHELXS-97/ SHELXT) and refined by full-matrix least-squares on F^2 (SHELXL-2014) (Sheldrick 2008) using the graphical user interface *ShelXle (Hübschle et al. 2011)*. All atoms in the room pressure structure and the high-pressure structures were refined isotropically. Because of their small scattering cross-sections, H atoms were not refined in the high-pressure structures. Complete crystallographic information files (CIFs) for each structure can be found in supplementary material, as well as a discussion on the selection of our unit cells.

Results and discussion

Ambient pressure luminescence spectra

The luminescence spectrum of dravite is characteristic of d^3 ions (e.g. Cr^{3+}, V^{2+}) in an intermediate strength crystal field (Tanabe and Sugano 1954). Both sharp and broad emission bands are observed at room temperature and 77 K at ambient pressures (Figure 2). Considering the similar concentrations of Cr and V in our sample (e.g. Cr: 215 ±19 ppm, V: 336 ±32 ppm), it is reasonable to assume that our steady state luminescence spectra contain overlapping bands from the emission of both Cr and V. This is commonly observed in emerald, which is the Cr and V rich variety of beryl (Ollier et al. 2015; O'Bannon and Williams 2016b). The intense and relatively sharp emission bands are commonly referred to as the R-lines and are associated with the spin-forbidden ^2E-$^4A_2$ transition, with the $^4A_2$ state being the ground state and the ^2E state being split in non-cubic environments (Syassen 2008), and the broad band emission is assigned to the spin-allowed $^4T_2$-$^4A_2$ transition (Sugano and Tanabe 1958; Burns 1993; Gaft et al. 2005).

At 300 K, three bands can be fit under the sharp emission bands and two can be fit under the broad portion of the spectrum at room temperature. At 77 K, the broad thermally populated $^4T_2$–associated bands are not entirely quenched, and four bands can be fit under the ^2E sharp emission bands. A detailed deconvolution of these sharp line emission bands at both room temperature and 77 K is given in the supplementary material (Figure S1). Dravite has two crystallographically unique octahedral sites, Al and Mg, and emission bands from both sites would likely be observed in steady state luminescence spectra. The simplest way for Cr^{3+} and V^{2+} to substitute into dravite is through isovalent substitutions (e.g. Cr^{3+} into Al^{3+} site and V^{2+} into Mg^{2+}). The four ~~deconvolved~~ deconvoluted components at 77 K thus can be attributed to two sets of R-lines, one set from Cr^{3+} and one from V^{2+}. The Al site in dravite is less distorted than the Mg site (Hawthorne et al. 1993, and this study), which would be expected to give rise to a narrower R-line splitting. Given the likely relative intensities of R_1 and R_2 and the anticipated relative splittings, we propose the following assignments: the Cr^{3+} R_1 band is likely located at 683.7 nm, with its R_2 band at 681.4 nm, and the V^{2+} R_1 band is at 686.4 nm and its associated R_2 band at 679.8 nm. This results in an R-line splitting of ~50 cm^{-1} for Cr^{3+} and ~143 cm^{-1} for V^{2+}. For comparison, ruby [Al_2O_3:Cr] has an Al-site that is close to an ideal octahedron with a slight trigonal distortion, and has an R-line splitting of ~29 cm^{-1} (Syassen 2008), while zoisite [$Ca_2Al_3Si_3O_{12}(OH)$] which has a highly distorted Al-site has an R-line splitting of ~340 cm^{-1} (Koziarska et al. 1994). The distortions of the Al and Mg sites in dravite fall intermediate between the distortions of the Al sites in ruby and zoisite, so these R-line splittings are plausible. To confirm the assignments of these emission bands, luminescence lifetime measurements or variably substituted samples would be required.

High-pressure luminescence spectra

High-pressure luminescence spectra are shown in Figure 3. Under compression the intensity of the R-lines decreases: this is likely primarily associated with the transition metal absorption bands migrating away from our excitation wavelength of 532 nm. Moreover, the disappearance of the broad $^4T_2$-associated band shows that a transition from an intermediate to strong crystal field occurs in the first few GPa of compression, which is consistent with previous observation in other Cr-bearing oxides (Dolan et al. 1986; de Viry et al. 1987; Hommerich and Bray 1995; Grinberg and Suchocki 2007; O'Bannon and Williams 2016b). As at 300 K, it is difficult to fit four bands under the ^2E region under compression, so we fit the spectra with three bands: based on our 77 K assignments, these are associated with the R_1 and R_2 peaks of Cr^{3+} and the R_1 peak of V^{2+}. Near 6.0 GPa, the primary emission feature fit by three bands clearly separates into individual peaks (Figure 3).

The pressure shift of two of the original three bands that were fit at ambient pressure and temperature shift negligibly--essentially by 0 nm/GPa up to ~9 GPa, while the other band shifts by 0.50 ±0.02 nm/GPa (-8.8 (±0.3) cm^{-1}/GPa) up to the same pressure (Figure 4a). The observation of effectively stationary emission bands under compression is without precedent among Cr^{3+} emission in oxides (e.g., Dolan et al. 1986; Mao et al. 1986; de Viry et al. 1987; Hommerich and Bray 1995; Grinberg and Suchocki 2007; O'Bannon and Williams 2016b). Above ~9.0 GPa, the initially stationary bands begin to shift positively in wavelength, towards lower energies (Figure 4b). The two bands that shift by 0 nm/GPa likely are associated with one octahedral site while the other band is produced by substitution in the other octahedral site.

This is in accord with our assignment of the former two bands to emission from Cr^{3+} substituting into the Al^{3+} site.

Four separate experiments were conducted in the ≤ 10.5 GPa range to assess the reproducibility of the unusual negligible pressure shift. It is completely reproducible, and no hysteresis is observed on decompression from ~10.5 GPa. The ~0 nm/GPa pressure shift suggests one of three possibilities. First, the crystallographic site that this band is emitting from may not be changing in volume under compression. Second, there may be a complex trade-off between electron density and volumetric change within the site. Third, an admixture of electronic states, rather than a pure ^2E -> $^4A_2$ transition, may generate the observed sharp-line emission. As described in the single-crystal diffraction section below, there is no structural "smoking gun" for this unusual pressure shift. Admixture of states (probably with the $^4T_2$ state) is a possibility; however, the troubling aspect of this explanation is that a pressure-induced shift in admixture must perfectly balance with the pressure shifts of the two states to produce a net zero pressure shift. Stated another way, the separation of the two states, their resulting admixture, and their pressure shifts must collectively sum to zero for ~9.0 GPa of compression. This scenario is quite unlikely because of the dramatically different pressure-dependences of the $^4T_2$ and ^2E states (e.g., O'Bannon and Williams 2016a), but could be testable with high-pressure lifetime measurements. A trade-off between changes in electron density and volumetric compaction is possible, but would require detailed insights into the bonding environment/electron density within the octahedral site under compression.

The splitting between these two bands also does not change on compression, suggesting that the site distortion is unchanged, as well. The change in slope at 9 GPa is, as described

below, likely not an indicator of a phase transition, but may represent a change in the compression mechanism. Moreover, the other observed emission band shifts positively in wavelength, consistent with the volume of this site decreasing with increasing pressure. Since we cannot deconvolutevе the expected R_2 component of this band in this pressure range, it is difficult to know from the emission spectra if this site becomes more or less distorted. However, the peakwidth of the positively shifting band slightly narrows under compression to ~9.0 GPa, which is an indicator that its site becomes less distorted under compression.

In the pressure range above 10 GPa, peak splitting is observed near 15 GPa, with new emission bands observed; at pressures above 45 GPa, non-linear pressure shifts are observed (Figure 3, 4b). No hysteresis is observed in the emission on decompression from 65 GPa, and the Raman spectrum of the decompressed sample is identical to the starting material. Peak splitting of emission bands under compression has been shown to be an indicator of phase transitions (O'Bannon and Williams 2016a,b). This is particularly anticipated when multiple octahedral environments are produced by a decrease in symmetry associated with a phase transition. For example, in the ring silicate beryl, the Cr^{3+} R-lines split into two sets of R-lines near 14.7 GPa (O'Bannon and Williams, 2016b) which agrees well with a theoretically predicted ~15 GPa soft-mode transition (Prencipe et al. 2011), as well as high-pressure single crystal diffraction studies which show that the Al-site splits into two crystallographically unique sites near 15 GPa (M. Merlini, personal communication). The peak splitting observed in dravite tourmaline under compression provides clear evidence that one of the octahedral sites splits into two unique sites (Figure 5).

The additional new bands at longer wavelength that appear above 10 GPa (Figures 3, 4b) are likely neighbor lines that are due to paired Cr-Cr emission (e.g., O'Bannon and Williams, 2017); vibronic lines may also lie at these wavelengths, but these typically do not dramatically exceed the zero-phonon lines in amplitude. The appearance of these new bands, and the progressive increase in their intensity with pressure may reflect: (1) the intensity of the broad $^4T_2$ transition has decreased substantially by this pressure and alternate mechanisms for emission are enhanced; (2) a change in the nearest neighbor configuration due to the splitting of one of the octahedral sites into two unique sites that produces configurations that favor energy transfer into and/or the magnetic interactions that generate emission from pairs; and/or (3) a pressure-induced shift in absorption that results in preferential excitation of pair-line emissions (e.g., O'Bannon and Williams 2017). Within the tourmaline structure, there are a wide range of possible prospective pair-wise magnetic interactions that could occur between substituents in the octahedral sites through an intervening anion, and it is well-known that the strength of such exchanges depends strongly on both the inter-ion distance and on the angle (e.g., McCarthy and Gudel 1988). Indeed, such pair-wise interactions between transition metals have long been recognized to be important within the optical spectrum of tourmalines (Mattson and Rossman 1987). Therefore, while the exact origin of the new bands and the shift in intensity above 10 GPa within the emission spectra remain unclear, it is probable that they can be attributed to pressure-enhanced pair-line emissions.

Thus, the major effects of compression on the luminescence spectrum are the change in pressure shift near 9.0 GPa and the peak splitting and increased intensities of new peaks observed at ~15 GPa. The lack of hysteresis on decompression from ~65 GPa indicates that any

phase transition associated with these changes is second order. We do not believe that the change observed at 9.0 GPa is produced by a pressure-induced structural phase transition, but is likely generated by either a change in compression mechanism or a progressive change in the electron density associated with the site. The changes observed at ~15 GPa are, however, consistent with a phase transition that involves a subtle distortion of the overall structure of dravite tourmaline that splits the Al-site into two unique sites. By analogy to high-pressure phase transitions in cordierite and beryl (Prencipe et al. 2011; Miletich et al. 2014; Finkelstein et al. 2015; O'Bannon and Williams 2016b), the structural change likely involves a modest distortion of the Si_6O_{18} ring away from hexagonal symmetry. Importantly, the overall topology of the structure appears to be preserved, and a lowering of symmetry from rhombohedral is unlikely. The presence of such a modest structural change implies that dravite tourmaline's metastability under room temperature compression to ~65 GPa is generated by the topology of the structure that stabilizes the Si_6O_{18} ring at high compressions. Moreover, a structural transition that involves a modest distortion of the Si_6O_{18} ring with no change in crystal system would be difficult to constrain with powder diffraction techniques (e.g., Li et al. 2004; Xu et al. 2016).

High-pressure single-crystal diffraction

To characterize the changes observed using luminescence spectroscopy, single crystal X-ray diffraction measurements were done at various pressures up to ~23.6 GPa. Dravite tourmaline indexes to a rhombohedral unit cell across the pressure range of the X-ray measurements. Structures solved as rhombohedral *R*3*m* up to ~15.4 GPa, and above this pressure the space group changed to *R*3. In the following sections, we discuss the equation of

state (EoS) for the low pressure phase of dravite tourmaline, and the high-pressure crystal structure of this material.

Dravite tourmaline EoS

Dravite tourmaline shows highly anisotropic compression (Figure 6), with the *c*-axis being substantially more compressible than the *a*-axis, which is in good agreement with the previous study of uvite tourmaline reported by Xu et al. (2016). Interestingly, Liu et al. (2004) report that the *c*-axis of schorl tourmaline is less compressible than the *a*-axis, which is opposite of what is observed in dravite and uvite tourmaline. But, the lattice parameters and unit cell volumes reported by Liu et al. (2004) are quite scattered. For clarity, we do not include these results in Figure 6, but they are included in supplementary Figure S2. The reason for the scatter in their data, and the difference in compressibility of the *a*- and *c*-axes is not clear, but could be a result of non-hydrostatic conditions of methanol:ethanol mixtures above ~10.5 GPa. We fit our pressure volume data with both 2nd and 3rd order Birch-Murnaghan equations of state (Table 1) using the EOSFit7GUI (Angel et al. 2014), and our results are shown in Table 2. An *F-f* plot based on the Birch-Murnaghan EoS fit of the volume data is shown in Figure S3. Our results indicate that dravite tourmaline is more compressible than uvite tourmaline. For comparison, the uvite sample measured by Xu et al. (2016) is not an endmember, but has ~10 % Na in the X-site, and pure uvite is likely less compressible than their measurements. The relatively large value for K_o reported for schorl tourmaline by Li et al. (2004) does not appear compatible with our results, nor with those of Xu et al. (2016).

High-pressure crystal structures

Structures were solved at various high pressures, and results of the structure refinements are shown in Table 3. The site volumes as a function of pressure show that the Na site is the most compressible (Figure 7). The Si site is the least compressible, while the two octahedral sites behave essentially identically to one another, and are intermediate in their compressibility between the Si and Na sites. Clearly, neither octahedral site volume is constant under compression. So, the unusual observation of a negligible pressure shift of two of the luminescence bands cannot be explained via a site volume argument alone. A more nuanced explanation for the shift of the energy levels, involving a shift in covalency/electron density of the site that counterbalances the volumetric compaction, appears necessary. The anisotropic compression of dravite tourmaline can be straightforwardly explained by the location of the Na site in the dravite structure and its large volume change under compression (Figure 7). Speculatively, the large volume change in the Na site could produce a pressure-induced reduction in the electron density around the Al-sites, such that their electron density remains fairly constant under compression up to ~9.0 GPa.

We calculate the distortion parameters for the octahedral and tetrahedral sites as a function of pressure (Supplementary Figure S4). Interestingly, the quadratic elongation (QE) and angle variance (AV) of the Mg site both decrease under compression, indicating that this site becomes less distorted under compression: this is in accord with our inference based on the width of the emission peak that we have assigned to this site. The Al site distortion changes by very little, and the Si site becomes slightly more distorted under compression. The Al-site distortion change is negligible, which also provides confirmation for our assignment of the two

emission bands with invariant positions that show no change in their splitting up to ~9.0 GPa to this site.

The X-site in tourmaline (the Na site in dravite) is typically considered a 9-fold coordinated site. Among the bond lengths associated with this site as a function of pressure (Figure 8), there are two unique bonds between the Na and the Si_6O_{18} ring (O5 and O4), and there is one unique bond between the Na and the Mg octahedra (O2). There is also a potential 10th coordinating oxygen atom (O1), and the distance to this oxygen atom is also shown in Figure 8. The O1 atom is, however, one of the two proton sites in tourmaline, although the H1 site has a very low reported occupancy (Gatta et al. 2014). F substitution also occurs only at the O1 site, and this site is influenced by cation occupancy of the *X* and *Y* sites (Henry and Dutrow 2011). Hence, O1 is not simply a simple oxygen site that appears to become bonded to the Na atom at high-pressure: rather, it is a site that is partially occupied by O, OH, and F. Interestingly, the two unique Na-O bonds to the Si_6O_{18} ring show different behaviors. Under compression to ~15.4 GPa, the Na-O4 bonds change by ~0.05 Å while the Na-O5 bonds change by ~0.25 Å. Over the same pressure range, the Na-O2 bonds change by ~0.11 Å. In this sense, the Na site appears to undergo the bulk of its compaction through six neighbors: three bonds into the Si_6O_{18} ring and three bonds into the Mg octahedra. This pseudo-six-fold behavior, with compacting connections to both the Mg polyhedra and the Si-ring, also sets up a natural way to distort the Si_6O_{18} ring away from hexagonal symmetry.

The B-O distances are less well-resolved, and change very little under compression but show a trend towards being more equidistant up to ~15.4 GPa (Supplementary Figure S5). In the high-pressure phase, B is surrounded by three crystallographically unique oxygen atoms (O8

splits into O8a and O8b). There is no indication that the BO_3 groups deviate from a planar configuration up to at least 23.6 GPa, which is expected given the spacegroups of the low- and high-pressure phases.

Compression mechanism

The compression mechanism of tourmaline involves a complex interplay of bond length shortening and oxygen atom displacement/rotation relative to its neighbors. Under compression the *Y*-site (MgO_6) volume decreases through Mg-O bond shortening and the distortion parameters of this site also decrease. As the volume of the *Y*-site decreases, the Si_6O_{18} ring becomes more puckered due to the displacement of the O6 atom towards the threefold rotation axis (Figure 9a). This increase in ring puckering has been observed in tourmaline when smaller cations are substituted into the *Y*-site. Bosi and Lucchesi (2007) report that the configuration of the six-membered ring is strongly affected by the average Y-O distance <Y-O> and, as <Y-O> decreases due to the substitution of smaller cations, the tetrahedra rotate around the O4-O5 edge and the O6 atom is displaced towards the threefold axis which produces puckering of the tetrahedral ring. Thus, chemical substitution of smaller cations into the *Y*-site and pressure appear to have the same effect on ring puckering.

As ring puckering increases under compression the O7 atom rotates towards the *Z*-site (AlO_6), which shortens the Al-O7 bond, and compresses the *Z*-site. This displacement of the O7 atom contributes to the increase in observed ring crimping under compression (Figure 9b), and the increase in ring crimping changes the O7-O8 edge distance. Crimping is defined as $\Delta Z = [{}_zO5-({}_zO4+{}_zO7)/2]*c$, where z is the coordinate of the oxygen atoms and *c* is the length of the *c*-axis (Gorskaya et al. 1982). From a chemical substitution perspective, it has been shown that

substitution into the *X*-site primarily affects the crimping and ditrigonality of the ring and distortion of the tetrahedra, while substitution into the *Y*-site primarily affects ring puckering (Foit, 1989). Ditrigonality increases across the pressure range of this single-crystal study (Figure 9c). It is defined as $\delta = (r_1 - r_s)/r_s$, where r_1 and r_s are the distances from O4 and O5, respectively, to the threefold axis (Barton 1969). Under compression, the Na site moves towards the ring, which also contributes to the increase in ring crimping and ditrigonality. Moreover, the overall distortion of the *Z*-site is primarily controlled by the size of the *Y*-site cation (Foit 1989). Therefore, it is not surprising that the distortion parameters of the *Z*-site show very little change under compression. Above ~15.4 GPa, tetrahedral rotation and ring puckering continue to increase while ring crimping decreases above the transition and then remains almost constant to the highest pressure of this study.

High-pressure phase transition

At pressures above 15.4 GPa, the structure of dravite tourmaline is solved as rhombohedral *R*3. The only difference in symmetry associated with this transition is the loss of a mirror plane in the high-pressure structure. The net result is that the Si, Al, O6, O7, and O8 sites all split into unique sites (Figure 10), which implies that the high-pressure phase of tourmaline is likely a higher entropy phase. Since the 3-fold rotation axis is preserved across this phase transition there is no change in the Mg, Na, or B sites. Importantly, this subtle crystallographic change is completely consistent with our luminescence observations of a second order phase transition occurring near ~15.4 GPa. Additionally, our assignment of the emission bands with an initial ~0 nm/GPa pressure shift to the Al site is a robust assignment. Interestingly, the slight distortion of the Si_6O_{18} ring preserves the overall topology of the tourmaline structure, while

providing a new deformation mechanism for the high-pressure phase. A plot of the Si-Si-Si angles shows that this angle deviates away from 120° above ~15.4 GPa and increases with increasing pressure up to ~23.6 GPa (Figure 11a). There is also a discontinuous shift in tetrahedral rotation, as well as a change in the pressure dependence of ring puckering and crimping above ~15.4 GPa (Figures 9b, 11). The deformation mechanism of the high-pressure phase primarily involves tetrahedral rotation and changes in the Si-Si-Si angles while ring crimping and puckering play less of a role. These subtle changes in ring distortion demonstrate the subtlety of this phase transition, and why it would be very difficult to resolve this type of phase transition with high-pressure powder diffraction techniques. Our luminescence data show that this high-pressure phase remains metastable under room temperature compression up to at least 65 GPa.

Speculatively, the high-pressure transition appears to be driven by steric/geometric effects caused by the decrease in volume of the *Y*-site and displacement of the *X*-site towards the Si_6O_{18} ring. As the *Y*-site volume decreases, the O6 atom is displaced towards the threefold axis causing ring puckering, which displaces the O7 atom towards the *Z*-site (Al), causing the Al-O7 distance to shorten which increases ring crimping. This causes a change in the tehtrahedral rotation of the SiO_4 tetrahedra, which breaks the mirror plane symmetry for O6 and O7. This change in rotation induces an additional twist on the MgO_6 and AlO_6 octahedra, which in turn tilts the BO_3 plane out of the plane normal to the rotation axis, and breaks the mirror symmetry of the O8 atom.

Na site coordination change?

The possible coordination change of the Na site merits discussion, as the topology of the tourmaline structure shows that the incipient Na1-O1 bond (Figure 8) provides the only straightforward means to further polymerize this structure. The distance to the potential 10th oxygen decreases by ~0.43 Å to 15.4 GPa, and the pressure dependence of its distance is constant above this pressure. Multiple phenomena could be at work here in changing the behavior of the Na-O bonds above the phase transition: (1) Na1 and O1 behave like they are bonded near the phase transition pressure (e.g. a coordination change of Na takes place); (2) repulsion increases between the O1 and O4, and O5 atoms; (3) an increase in repulsion between H1 and Na1 occurs near 15.4 GPa, which results in a shortening of the O1-H1 bond, and/or a change in H-bonding configuration; and/or (4) the compression mechanism of the high-pressure phase is different than the low pressure phase.

Considering the mixed occupancy of the O1 site (e.g. Gatta et al., 2014; Henry and Dutrow, 2011; Bosi, 2018), it is unlikely a bond is forming between Na and O1. A plot of O-O distances reveals that there are no systematic trends that would suggest that the change in pressure dependence of the Na-O1 distance is due to an increase in O-O repulsion (supplementary Figure S6). It has been reported that an increase in size of the *X*-site cation results in an expansion of the X-site coordination polyhedron, which impinges on the hydroxyl at the O1 site, leading to a shortening of the O1-H1 bond (Berryman et al., 2016). It is possible that above ~15.4 GPa, an increase in Na-H repulsion occurs that results in a shortening of the O-H bond which changes the pressure dependency of the Na1-O1 distance. However, due to the low reported occupancy of H1 this seems unlikely. As discussed above, ring puckering and crimping also behave differently in the high-pressure phase, indicating that compression mechanisms

shift in the high-pressure phase. Thus, a change in compression mechanism is the most plausible explanation for the change in Na1-O1 pressure dependence that is observed above ~15.4 GPa.

Bond Valence Analysis

We quantitatively analyze the stability of the dravite tourmaline structure using the bond valence approach (Brown, 2002). The bond valence approach has been extensively deployed to examine the structural changes in tourmalines due to chemical variability at ambient conditions (Fortier and Donnay, 1975; Hawthorne et al., 1993; Hawthorne, 1996; Hawthorne, 2002; Bosi and Lucchesi, 2007). We first use the relative deviation of the bond valence sum from the ideal value ($\Sigma(S_{ij}) - v_i)/v_i$) for all cations and anions to quantify the steric stress of the structure at ambient condition. Here, S_{ij} is the bond valence between atoms *i* and *j*, and v_i is the absolute value of atom *i*'s valence. The bond valence sums are shown in Figure 12 on the ordinate (i.e. the zero-pressure values). It is striking that even at ambient conditions, the Mg cation is overbonded by almost 20 %. This is due to the MgO_6 octahedron sharing two edges in cis-conformation with the AlO_6 octahedron. The relaxed cation-oxygen distances for Al^{3+} and Mg^{2+} differ by about 10% (1.9 vs 2.1 Å). Thus, each MgO_6 shares two edges with an AlO_6 octahedron, whereas each AlO_6 octahedron shares one edge with a MgO_6 octahedra. As a consequence, Mg shows an almost 20% overbonding while AlO_6 is underbonded, albeit to a smaller extent (~ 3%).

In terms of the bond valence sums as a function of pressure (Figure 12), two features stand out: Na (which at ambient pressure is slightly underbonded) increases its overbonding by a remarkable 70%. Mg, which starts out at almost 20% overbonded increases to about 40% by

215 GPa, at which pressure it then levels out. Notably, Na and Mg are the two cations with the weakest individual bonds. All other cations show a shallow increase in overbonding, which increase moderately to a maximum of 20% at the highest pressures. The same general increase holds for the oxygen atoms, which are all tightly bunched together at values below 20 % (we disregard O1 and O3 here because the poorly constrained hydrogen positions make their bond valence sums ill defined).

The weakly bonded Na and Mg cations seem to be dramatically overbonded at high pressures, without affecting significantly ~~effect on~~ the stability of the tourmaline structure (beyond the modest descent of symmetry near 15 GPa). This stability of the structure may be rooted in none of the oxygen atoms being overbonded by more than 20 % up to the highest pressure of ~24 GPa. Consequently, we hypothesize that this high-pressure stability of the tourmaline structure is closely tied to its extraordinary structural tolerance with respect to chemical substitutions on the *X*, *Y*, and *Z* sites. The bond network of tourmaline seems to have the ability to balance the modest overbonding of the oxygen atoms which hold the framework together, in spite of the significant overbonding on the most weakly bonded metal ions.

Indeed, the subtle mirror plane breaking phase transition observed above ~15.4 GPa is not reflected in the bond valence analysis. Instead, this phase transition is likely due to a steric/geometric effect caused by a complex interplay of bond length shortening and oxygen atom rotation/displacement which alter ring puckering, ring crimping, tetrahedral rotation, and ditrigonality. As the ring distortion parameters change under compression, mirror plane symmetry is broken for O6, O7, and O8. Hence, there does not appear to be an obvious

villain(s) that drives the transition from *R*3*m* to *R*3; it is perhaps best viewed as a cooperative instability of the (initially) hexagonal ring configuration, via its interactions with the Y (Na) cation.

Implications

Other compositions of tourmaline that are rhombohedral *R*3*m* at room temperature and pressure will likely behave similarly, and undergo a similar transition, under compression. The main difference is likely to be the pressure at which the *R*3*m* to *R*3 transition occurs. Tourmaline is a complex mineral group, and the high-pressure behavior of tourmalines with extensive Li, Cr, or V substitution into the *Y* and *Z* sites, Pb substitution into the *X*-site, or Al, Li substitution into the *T*-sites could be quite different than that of tourmalines with predominantly Al and Mg in their *Y* and *Z* sites. Nevertheless, the main chemical control over the pressure at which this transition occurs is likely the identity of the cation in the X-site. Here, simple systematics would indicate that a larger cation would generate this distortion at lower pressure conditions. Thus, the pressures of this transition in uvite tourmaline [$Ca(Mg_3)MgAl_5(Si_6O_{18})(BO_3)_3(OH)_3(OH)$] and maruyamaite tourmaline [$K(MgAl_2)(Al_5Mg)(BO_3)_3(Si_6O_{18})(OH)_3O$] are expected to be higher and lower than in dravite tourmaline, respectively. Moreover, our high-pressure results show that massive overbonding of the *X* and *Y* sites can be accommodated by the tourmaline structure. This unexpected result may explain the extraordinary structural tolerance with respect to chemical substitution on the *X*, *Y*, and *Z* sites. Hence, any over/underbonding due to chemical substitutions is balanced by the topology of the tourmaline structure, and perhaps in particular the oxygen atoms.

The crystallization conditions of metamorphic tourmaline are complex, but one means of crystallization involves consuming B that is released during clay and mica mineral dehydration reactions (Ota et al. 2007). Hence, tourmaline is likely present in subduction zones where sedimentary rocks are being subducted. Petrologic studies have shown that dravite tourmaline breaks down at ~7.0 GPa and ~900 °C (Werding and Schreyer 1996) and ~3-5 GPa and ~1000 °C (Krosse 1995). However, tourmaline stability is highly dependent on compositional variations (e.g. its Mg/[Fe+Mg] ratio, Na, Al and B contents), coexisting fluids and the host rock (Henry and Dutrow, 1996; Dutrow et al., 1999; Schreyer, 2000; Ota et al. 2008). The higher pressure/lower temperature stability of dravite tourmaline is not well constrained (see figure 2b in Ota et al. 2007). Moreover, tourmaline has a greatly diminished stability range in SiO_2 saturated systems with common pelitic compositions, and even in relatively cold subduction zones, tourmaline breaks down by ~150 km depth (Ota et al. 2008). Hence, the commonly invoked “cold subduction zone” argument for the stability of tourmaline appears to be invalid. A complete understanding of the host rock chemistry, redox conditions, and pressure and temperature conditions are required to truly constrain the stability field of tourmaline supergroup minerals in subduction zones. The stability fields of dravite tourmaline and other varieties of tourmaline are not well constrained, and neither the onset pressure of the symmetry-lowering transition in other varieties of tourmaline, nor its temperature-dependence is known. Thus, it is unclear whether the high-pressure phase of dravite or other compositions of tourmaline would be found at depth within subduction zones.

Acknowledgments

We thank Simon Teat and Nico Giordano from Beamline 11.3.1 at the ALS. We also thank Rob Franks for help with LA-ICPMS measurements and Dan Sampson for help with the Raman spectrometer. A portion of this work was performed under the auspices of the US Department of Energy by Lawrence Livermore National Laboratory under Contract No. DE-AC52-07NA27344. Work partially supported by NSF through EAR-1620423 and COMPRES under NSF Cooperative Agreement EAR-1606856. The Advanced Light Source is supported by the Director, Office of Science, Office of Basic Energy Sciences, of the U.S. Department of Energy under contract DE-AC02-05CH11231.

References

Akizuri, M., Kuribayashi, T., Nagase, T., and Kitakaze, A. (2001) Triclinic liddicoatite and elbaite in growth sectors of tourmaline from Madagascar. American Mineralogist, 86, 364–369.

Angel, R.J., Gonzalez-Platas, J., and Alvaro, M. (2014) EosFit7c and a Fortran module (library) for equation of state calculations. Zeitschrift fur Kristallographie, 229, 405–419.

Bebout, G., and Nakamura, E. (2003) Record in metamorphic tourmalines of subduction-zone devolatilization and boron cycling cycling Record in metamorphic tourmalines of subduction-zone devolatilization and boron cycling. Geology, 31, 407–410.

Berryman, E. J., Wunder, B., Ertl, A., Koch-Müller, M., Rhede, D., Scheidl, K., Giester, G., & Heinrich, W. (2016). Influence of the X-site composition on tourmaline's crystal structure: investigation of synthetic K-dravite, dravite, oxy-uvite, and magnesio-foitite using SREF and Raman spectroscopy. Physics and Chemistry of Minerals, 43, 83-102.

Boehler, R., and De Hantsetters, K. (2004) New anvil designs in diamond-cells. High Pressure Research, 24, 391–396.

Bosi, F., (2018) Tourmaline crystal chemsitry. American Mineralogist, in press.

Bosi, F., & Lucchesi, S. (2007). Crystal chemical relationships in the tourmaline group: Structural constraints on chemical variability. American Mineralogist, 92, 1054-1063.

Brown, I.D. (2002) The chemical bond in inorganic chemistry. Oxford University Press, Oxford.

Burns, R.G. (1993) Mineralogical applications of crystal field theory, 2nd Ed., Cambridge University press, 575 pp.

Chervin, J.C., Canny, B., and Mancinelli, M. (2001) Ruby-spheres as pressure gauge for optically transparent high pressure cells. High Pressure Research, 21, 305–314.

de Viry, D., Denis, J.P., Tercier, N., and Blanzat, B. (1987) Effect of pressure on trivalent chromium photoluminescence in fluoride garnet $Na_3In_2Li_3F_{12}$. Solid State Communications, 63, 1183–1188.

Dolan, J.F., Kappers, L.A., and Bartram, R.H. (1986) Pressure and temperature dependence of chromium photoluminescence in $K_2NaGaF_6:Cr^{3+}$. Physical Review B, 33, 7339–7341.

Domanik, K.J., and Holloway, J.R. (1996) The stability and composition of phengitic muscovite and associated phases from 5.5 to 11 GPa: Implications for deeply subducted sediments. Geochimica et Cosmochimica Acta, 60, 4133–4150.

Dutrow, B.L., Foster, C.T. Jr., and Henry, D.J., (1999) Tourmaline -rich psuedomorphs in sillimanite zone metapelites: demarcation of an infilteration front. American Mineralogist, 84, 794-805.

Finkelstein, G.J., Dera, P.K., and Duffy, T.S. (2015) High-pressure phases of cordierite from single-crystal X-ray diffraction to 15 GPa. American Mineralogist, 100, 1821–1833.

Fortier, S., & Donnay, G. (1975). Schorl refinement showing composition dependence of the tourmaline structure. The Canadian Mineralogist, 13, 173-177.

Frondel, C. (1948) Tourmaline pressure gauges. American Mineralogist, 33, 1–17.

Gaft, M., Reisfeld, R., and Panczer, G. (2005) Modern Luminescence Spectroscopy of Minerals and Materials, 356 p. Springer-Verlag, Berlin.

Gasharova, B., Mihailova, B., and Konstantinov, L. (1997) Raman spectra of various types of tourmaline. European Journal of Mineralogy, 9, 935–940.

Gatta, G. D., Bosi, F., McIntyre, G. J., & Skogby, H. (2014). First accurate location of two proton sites in tourmaline: A single-crystal neutron diffraction study of oxy-dravite. Mineralogical Magazine, *78*, 681-692.

Grinberg, M., and Suchocki, A. (2007) Pressure-induced changes in the energetic structure of the $3d^3$ ions in solid matrices. Journal of Luminescence, 125, 97–103.

Hamburger, G.E., and Buerger, M.J. (1948) The structure of tourmaline. American Mineralogist, 33, 532–540.

Hawthorne, F. C. (1996). Structural mechanisms for light-element variations in tourmaline. The Canadian Mineralogist, 34, 123-132.

Hawthorne, F. C. (2002). Bond-valence constraints on the chemical composition of tourmaline. The Canadian Mineralogist, 40, 789-797.

Hawthorne, F. C., & Dirlam, D. M. (2011). Tourmaline the indicator mineral: From atomic arrangement to Viking navigation. Elements, 7, 307-312.

Hawthorne, F.C., and Henry, D.J. (1999) Classification of the minerals of the tourmaline group. European Journal of Mineralogy, 11, 201–216.

Hawthorne, F.C., Macdonald, D.J., and Burns, P.C. (1993) Reassignment of cation site occupancies in tourmaline: Al-Mg disorder in the crystal structure of dravite. American Mineralogist, 78, 265–270.

Henry, D. J., & Dutrow, B. L. (2011). The incorporation of fluorine in tourmaline: Internal crystallographic controls or external environmental influences?. The Canadian Mineralogist, 49, 41-56.

Henry, D. J., & Dutrow, B. L. (1996). Metamorphic tourmaline and its petrologic applications. Reviews in Mineralogy and Geochemistry, *33*, 503-557.

Henry, D.J., Novák, M., Hawthorne, F.C., Ertl, A., Dutrow, B.L., Uher, P., and Pezzotta, F. (2011) Nomenclature of the tourmaline-supergroup minerals. American Mineralogist, 96, 895–913.

Hommerich, U., and Bray, K.L. (1995) High-pressure laser spectroscopy of Cr^{3+}:$Gd_3Sc_2GaO_{12}$ and Cr^{3+}:$Gd_3Ga_5O_{12}$. Physical Review B, 51, 12133–12141.

Hübschle, C.B., Sheldrick, G.M., and Dittrich, B. (2011) ShelXle: A Qt graphical user interface for SHELXL. Journal of Applied Crystallography, 44, 1281–1284.

Hughes, J.M., Ertl, A., Dyar, M.D., Grew, E.S., Shearer, C.K., Yates, M.G., and Guidotti, C. V. (2000) Tetrahedrally coordinated boron in a tourmaline: Boron-rich olenite from Stoffhutte, Koralpe, Austria. Canadian Mineralogist, 38, 861–868.

Ito, T., and Sadanaga, R. (1951) A Fourier analysis of the structure of tourmaline. Acta Crystallographica, 4, 385–390.

Kantor, I., Prakapenka, V., Kantor, A., Dera, P., Kurnosov, A., Sinogeikin, S., Dubrovinskaia, N., and Dubrovinsky, L. (2012) BX90: A new diamond anvil cell design for X-ray diffraction and optical measurements. Review of Scientific Instruments, 83, 125102.

Klotz, S., Chervin, J.-C., Munsch, P., and Le Marchand, G. (2009) Hydrostatic limits of 11 pressure transmitting media. Journal of Physics D: Applied Physics, 42, 75413.

Koziarska, B., Godlewski, M., Suchocki, A., Czaja, M., and Mazurak, Z. (1994) Optical properties of zoisite. Physical Review B, 50, 297–300.

Krosse, S. (1995) Hochdrucksynthese, stabilitat und eigenschaften der borsilikate dravit und kornerupin sowie darstellung und stabilitatsverhalten eines neuen Mg-Al-borates. Doctor thesis, Ruhr-Universita ¨t, Bochum.

Kunz, M., & Brown, I. D. (1995). Out-of-center distortions around octahedrally coordinated d^0 transition metals. Journal of Solid State Chemistry, *115*, 395-406.

Lameiras, F.S., Nunes, E.M.H. & Leal, J.M. (2010) Backgrounds for the industrial use of black tourmaline based on its crystal structure characteristics. Ferroelectrics, 377, 107-119.

Li, H., Qin, S., Zhu, X., Liu, J., Li, X., Wu, X., and Wu, Z. (2004) In situ high-pressure X-ray diffraction of natural tourmaline. Nuclear Techniques, 27, 919–922.

Mao, H.K., Xu, J.A., and Bell, P.M. (1986) Calibration of the ruby pressure gauge to 800 kbar under quasi-hydrostatic conditions. Journal of Geophysical Research, 91, 4673–4676.

Marschall, H.R., Altherr, R., and Rüpke, L. (2007) Squeezing out the slab - modelling the release of Li, Be and B during progressive high-pressure metamorphism. Chemical Geology, 239, 323–335.

Mattson, S.M. and Rossman, G.R. (1987) Fe^{2+}-Fe^{3+} interactions in tourmaline. Physics and

Chemistry of Minerals, 14, 163-171.

McCarthy, P.J. and Gudel, H.U. (1988) Optical spectroscopy of exchange-coupled transition metal complexes. Coordination Chemistry Reviews, 88, 69-131.

Miletich, R., Gatta, G.D., Willi, T., Mirwald, P.W., Lotti, P., and Merlini, M. (2014) Cordierite under hydrostatic compression: Anomalous elastic behavior as a precursor for a pressure-induced phase transition. American Mineralogist, 99, 479–493.

Nakano, T., and Nakamura, E. (2001) Boron isotope geochemistry of metasedimentary rocks and tourmalines in a subduction zone metamorphic suite. Physics of the Earth and Planetary Interiors, 127, 233–252.

Novák, M., Henry, D., Hawthorne, F. C., Ertl, A., Uher, P., Dutrow, B., & Pezzotta, F. (2009). Nomenclature of the tourmaline-group minerals. Report of the subcommittee on tourmaline nomenclature to the International Mineralogical Association's Commission on New Minerals, Nomenclature and Classification, CNMMN, pp. 1-45.

O'Bannon, E.F. and Williams, Q. (2016a) A Cr^{3+} luminescence study of spodumene at high pressures: Effects of site geometry, a phase transition, and a level crossing, American Mineralogist, 101, 1406-1413.

O'Bannon, E.F. and Williams, Q. (2016b) Beryl-II, a high-pressure phase of beryl: Raman and luminescence spectroscopy to 16.4 GPa. Physics and Chemistry of Minerals, 43, 671-687.

O'Bannon, E.F. and Williams, Q. (2017) Delocalization in Cr^{3+} luminescence of clinochlore: A pressure-induced transition from single-ion emission to pair emission, Journal of Physics and Chemistry of Solids, 109, 89-99.

Ollier, N., Fuchs, Y., Cavani, O., Horn, A.H., and Rossano, S. (2015) Influence of impurities on Cr^{3+} luminescence properties in Brazilian emerald and alexandrite. European Journal of Mineralogy, 27, 783–792.

Ota, T., Kobayashi, K., Katsura, T., and Nakamura, E. (2008) Tourmaline breakdown in a pelitic system: Implications for boron cycling through subduction zones. Contributions to Mineralogy and Petrology, 155, 19–32.

Parsons, S. (2010) ECLIPSE - Program for masking high-pressure diffraction images and conversion between CCD image formats.

Piermarini, G., Block, S., and Barnett, J. (1973) Hydrostatic limits in liquids and solids to 100 kbar. Journal of Applied Physics, 44, 5377-5382.

Prencipe, M., Scanavino, I., Nestola, F., Merlini, M., Civalleri, B., Bruno, M., and Dovesi, R. (2011) High-pressure thermo-elastic properties of beryl ($Al_4Be_6Si_{12}O_{36}$) from ab initio calculations, and observations about the source of thermal expansion. Physics and Chemistry of Minerals, 38, 223–239.

Robinson, K., Gibbs, G.V., and Ribbe, P.H. (1971) Quadratic elongation : A quantitative measure of distortion in coordination polyhedra. Science, 172, 567–570.

Rosenberg, P.E., and Foit, F.F. (1979) Synthesis and characterization of alkali-free tourmaline. American Mineralogist, 64, 180–186.

Scheidl, K.S., Gatta, G.D., Pippinger, T., Schuster, B., Trautmann, C., and Miletich, R. (2014) Static elasticity of cordierite I: Effect of heavy ion irradiation on the compressibility of hydrous cordierite. Physics and Chemistry of Minerals, 41, 579–591.

Schreyer, W. (2000) Is the partitioning of boron between tourmaline and muscovite dependent on the crystallization environment? J Czech Geol Soc 45:13–20

Shekhar Pandey, C., and Schreuer, J. (2012) Elastic and piezoelectric constants of tourmaline single crystals at non-ambient temperatures determined by resonant ultrasound spectroscopy. Journal of Applied Physics, 111, 013516.

Sheldrick, G.M. (2008) A short history of SHELX. Acta crystallographica. Section A, Foundations of crystallography, 64, 112–22.

Shtukenberg, A., Rozhdestvenskaya, I., Frank-Kamenetskaya, O., Bronzova, J., Euler, H., Kirfel, A., Bannova, I., and Zolotarev, A. (2007) Symmetry and crystal structure of biaxial elbaite-liddicoatite tourmaline from the Transbaikalia region, Russia. American Mineralogist, 92, 675–686.

Sugano, S., and Tanabe, Y. (1958) Absorption Spectra of Cr3+ in Al2O3 Part A. Theoretical Studies of the absorption Bands and Lines. Journal of the Physical Society of Japan, 13, 880–889.

Syassen, K. (2008) Ruby under pressure. High Pressure Research, 28, 75–126.

Tanabe, Y., and Sugano, S. (1954) On the Absorption Spectra of Complex Ions. I. Journal of the Physical Society of Japan, 9, 753–766.

Werding, G., and Schreyer, W. (1996) Experimental studies on borosilicates and selected borates. Reviews in Mineralogy and Geochemistry, 33.1, 117–163.

Xu, J., Kuang, Y., Zhang, B., Liu, Y., and Fan, D. (2016) Thermal equation of state of natural tourmaline at high pressure and temperature. Physics and Chemistry of Minerals.

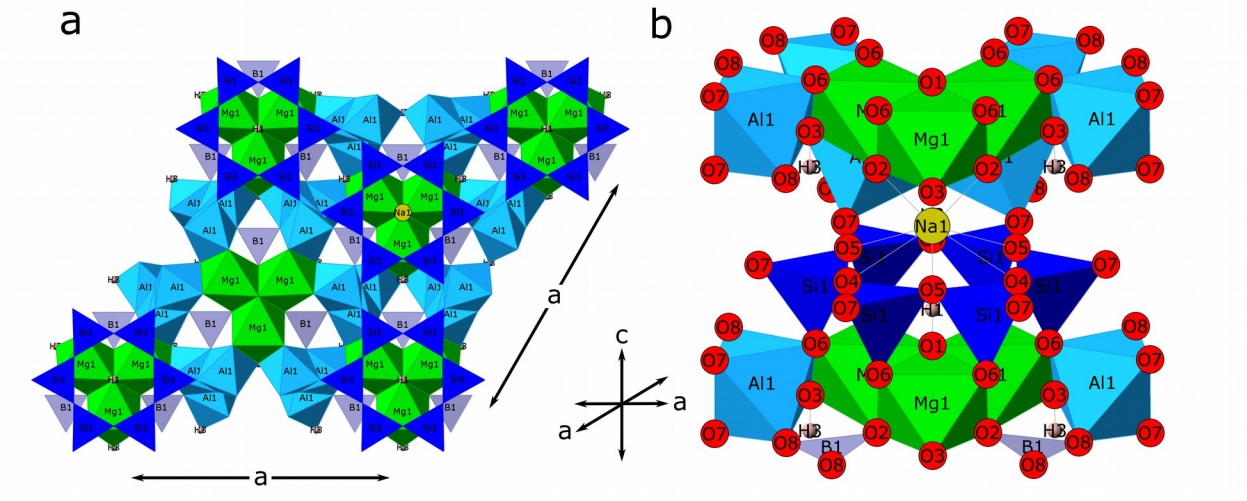

725

726

727Figure 1. Our room pressure crystal structure diagram of dravite tourmaline. (a) looking down
728the *c*-axis with oxygens removed for clarity. (b) oblique view showing the configuration of the X-
729site within the Si_6O_{18} ring. Modified after Hawthorne and Dirlam (2011). Diagrams were
730generated in CrystalMaker ® v8.7.6.

731

732

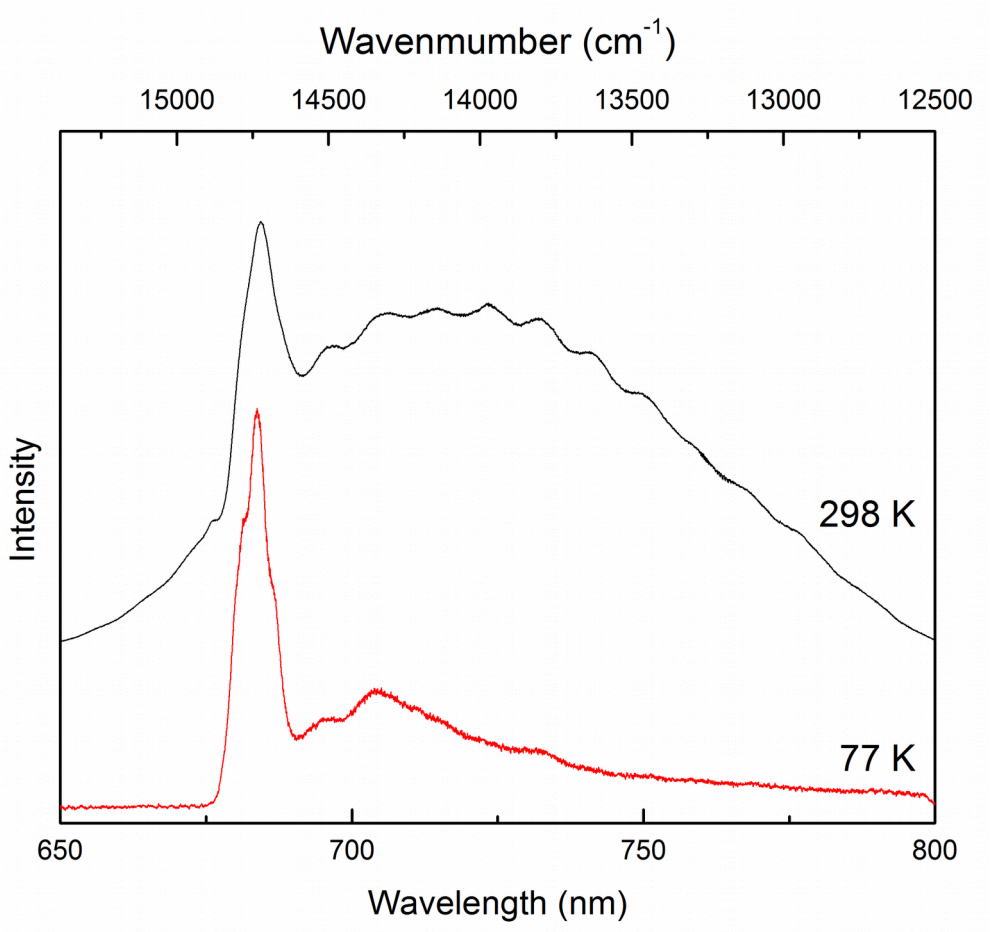

733

734Figure 2. Steady state luminescence spectra of dravite tourmaline at 300 and 77 K using 532nm
735excitation. Note that the thermally populated $^4T_2$ bands are not entirely quenched at 77K. The
736modulation in the broad band emission band at 300 K is an artifact.

737

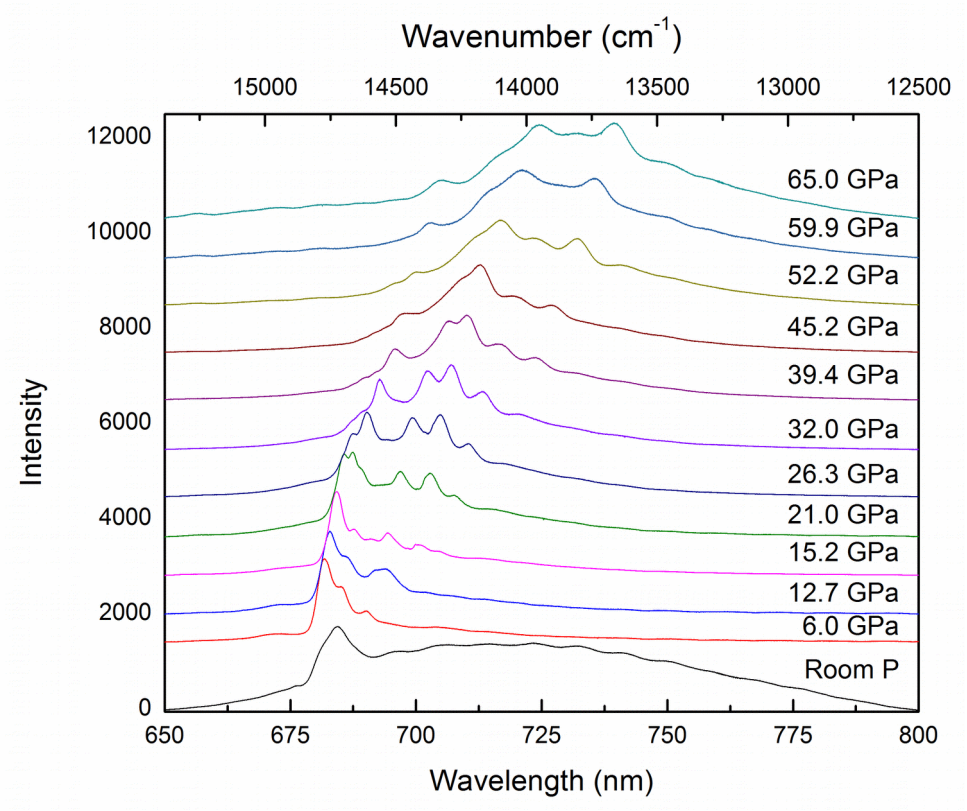

738

739Figure 3. High-pressure luminescence spectra of dravite tourmaline up to 65 GPa in a Ne
740pressure medium. The transition from intermediate to strong crystal field occurs between room
741pressure and ~6.0 GPa, as manifested by the decline in intensity of the broad-band $^4T_2$ emission
742centered near 725 nm.

743

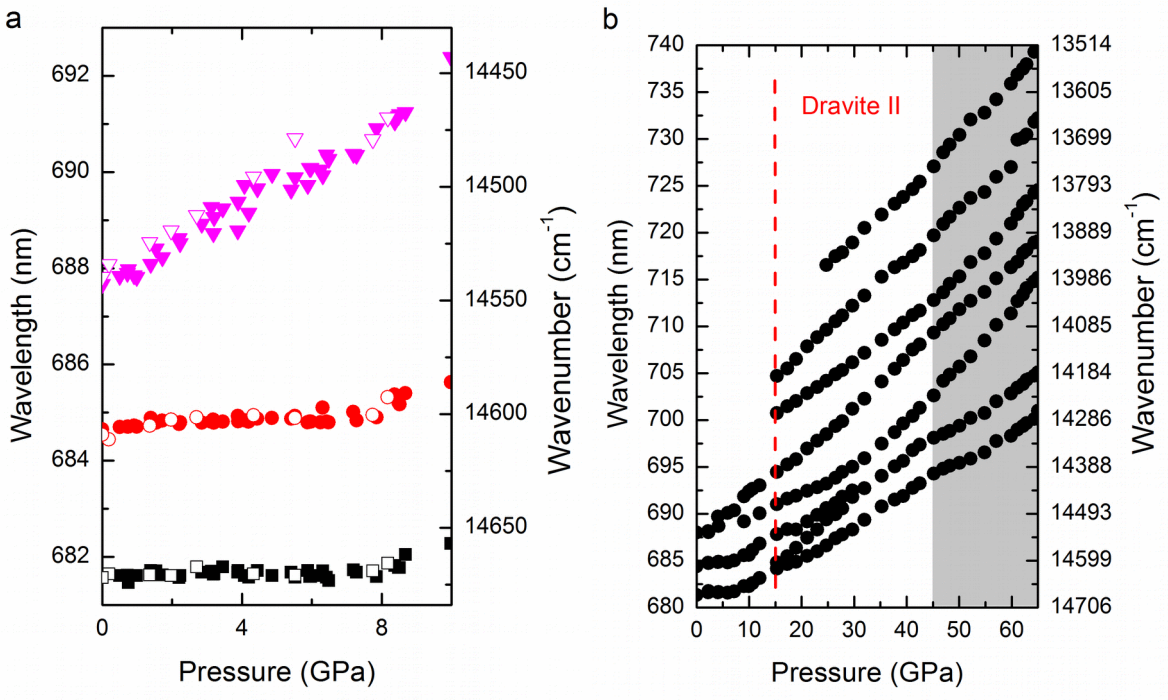

744

745Figure 4. Pressure shift of the observed luminescence bands in dravite (a) low pressure region,
746showing the essentially 0 nm/GPa pressure shift of two of the emission bands; and (b) up to 65
747GPa. The grey region indicates a possible change in compression mechanism. Closed symbols
748are data collected on compression, and open symbols are on decompression (for clarity, these
749are not included in b). Error bars are smaller than the symbols.

750

751

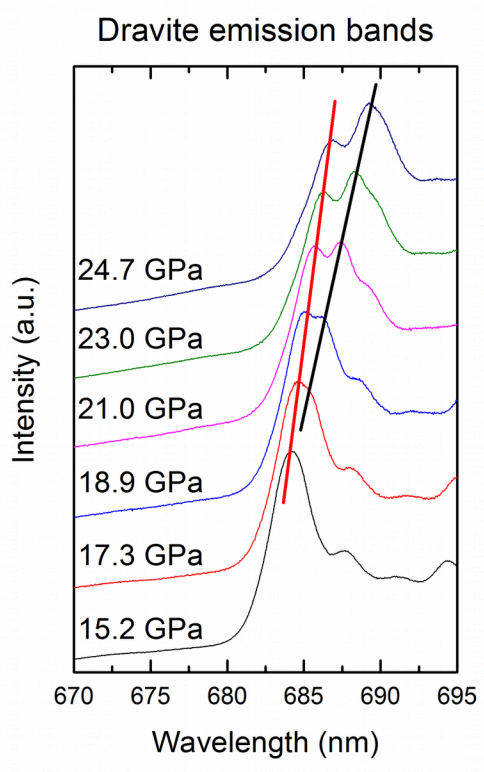

752

753Figure 5. Detail of dravite R-related emission band illustrating the splitting observed under
754compression.

755

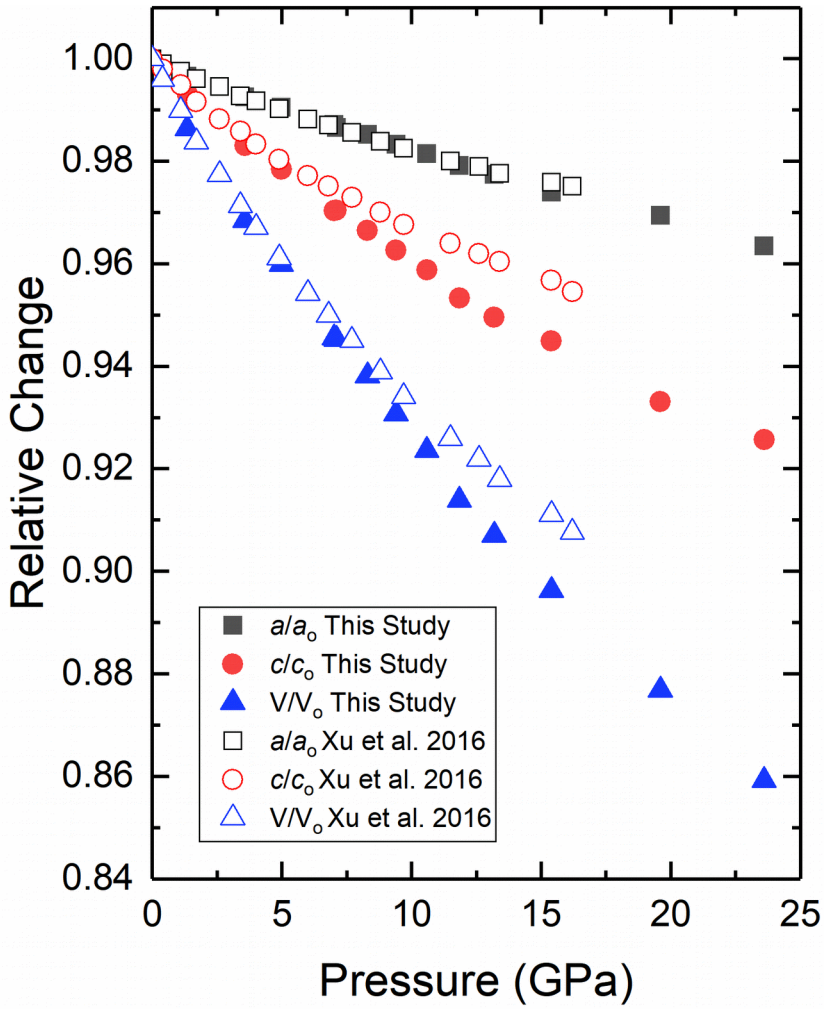

Figure 6. Relative change of lattice parameters and unit cell volume for uvite (Xu et al. 2016), and dravite (this study). The results of Li et al. (2004) are not plotted for clarity (see Supplementary Information). Error bars for our study are smaller than the symbols.

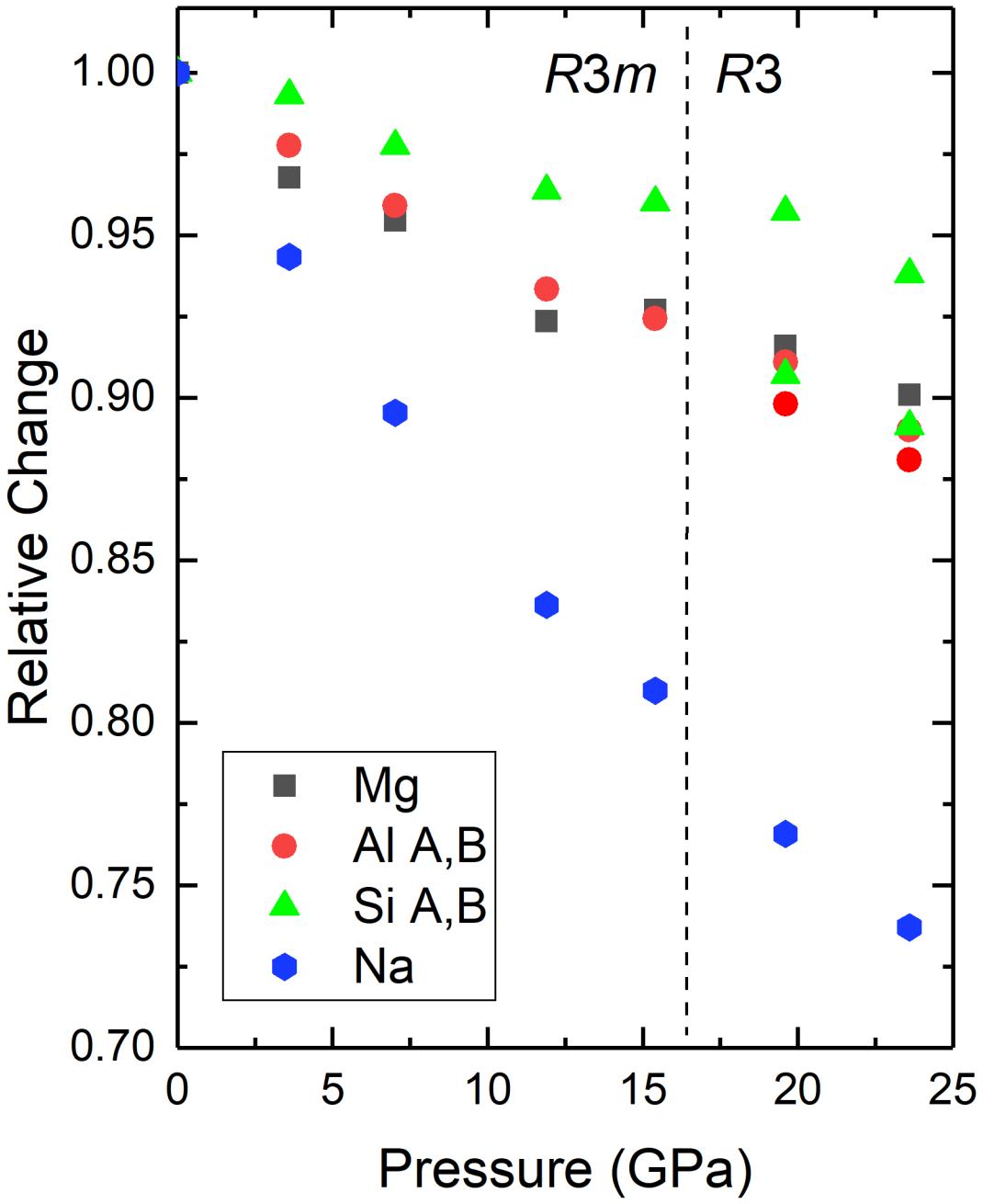

762
763
764Figure 7. Site volumes in dravite tourmaline as a function of pressure. There is a large difference
765in compressibility between the Na site and the Si, Al, and Mg sites. Note that the Na site is
766considered 9-fold across the pressure range of these measurements.
767

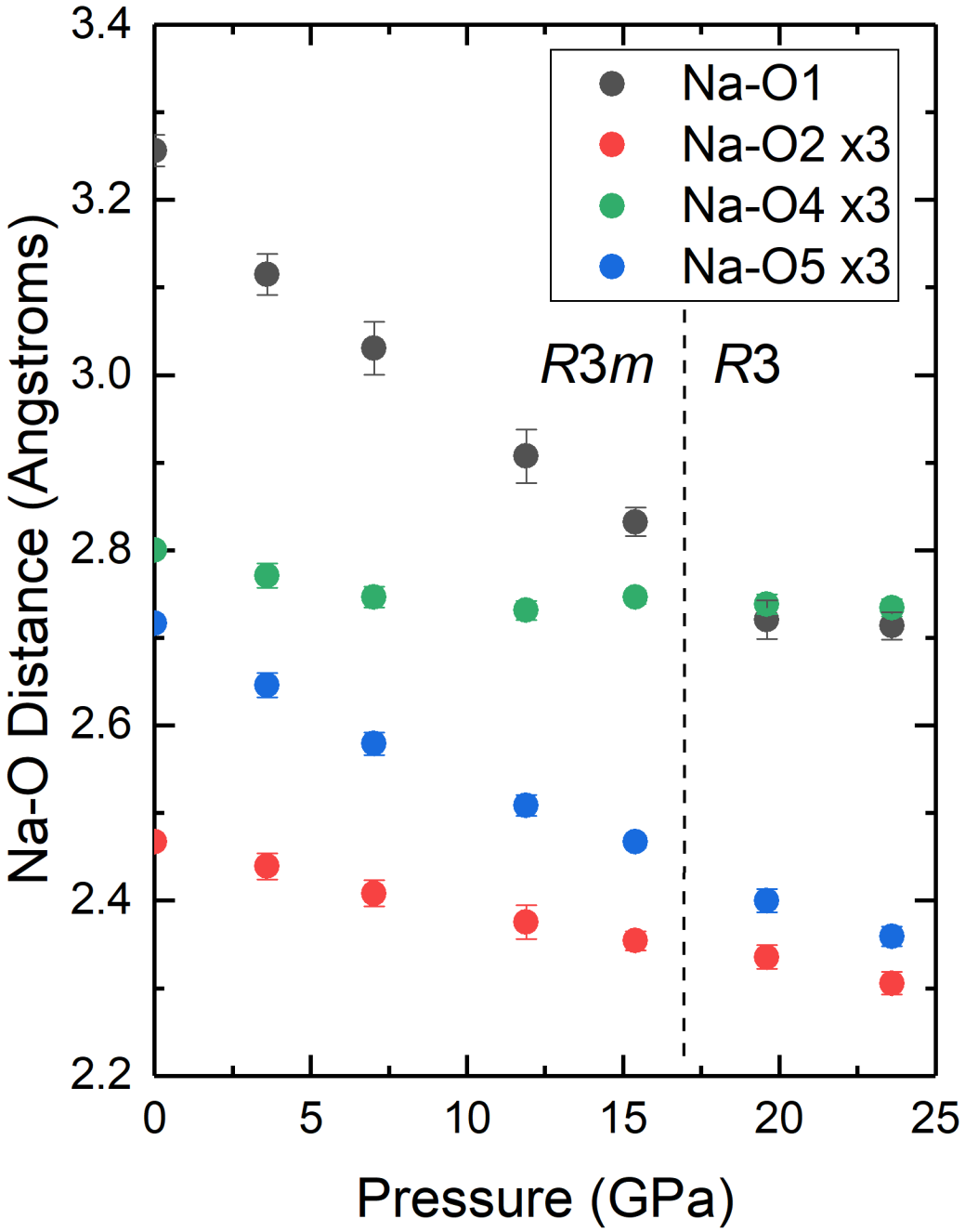

Figure 8. Na-O bond lengths of dravite tourmaline as a function of pressure. Note the different behavior of the two sets of three Na-O-Si bonds, and the change in slope of the Na-O1 distance above ~15.4 GPa.

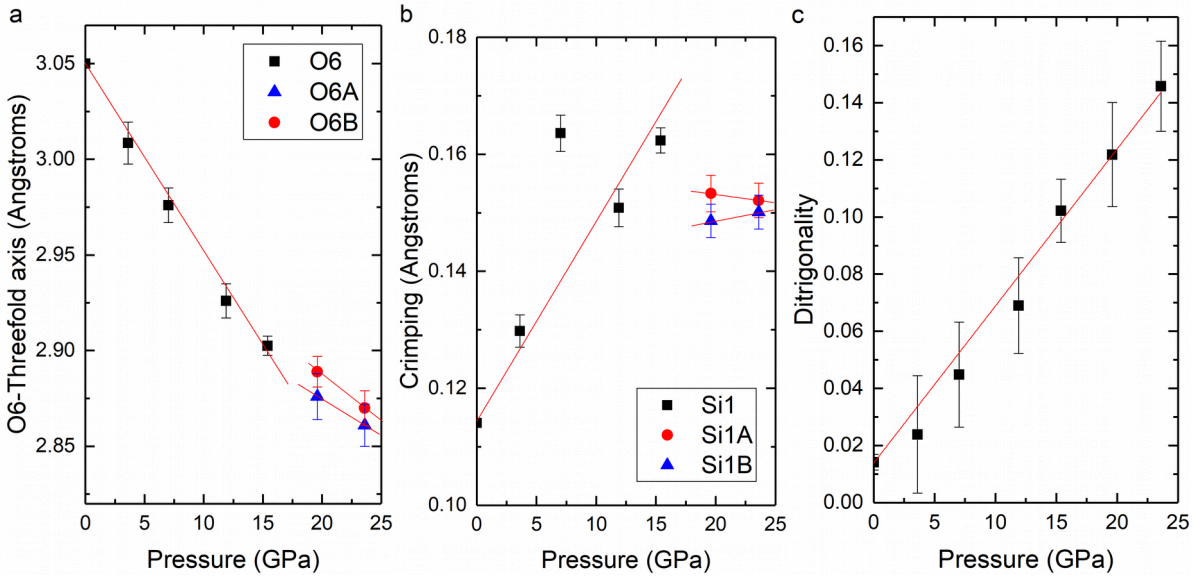

Figure 9. Ring distortion parameters as a function of pressure: (a) O6-threefold axis distance as a function of pressure (e.g. ring puckering). This distance decreases as pressure increases, indicating that ring puckering increases as pressure increases. (b) Ring crimping (see text for definition), showing the change in ring crimping in the high-pressure phase. (c) Ditrigonality (see text). The change in puckering and crimping in the high-pressure phase indicate that the compression mechanism changes in the high-pressure phase.

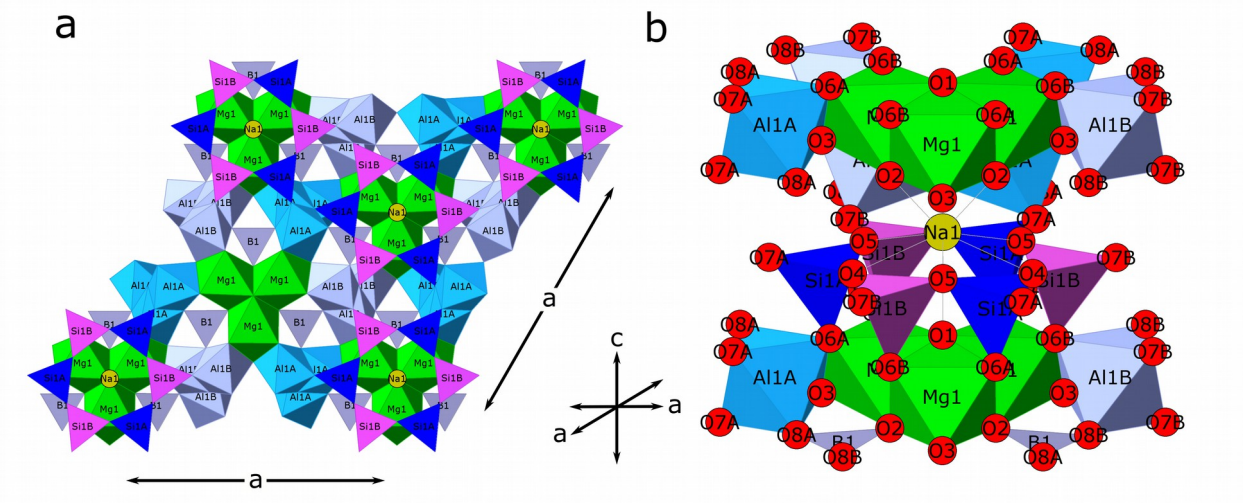

Figure 10. Our 23.6 GPa *R*3 structure of dravite tourmaline. (a) looking down the *c*-axis with oxygens removed for clarity. (b) oblique view showing the configuration of the *X*-site within the Si_6O_{18} ring. Note that Al, Si, O6, O7, and O8 all split into unique sites in the high-pressure phase. Diagrams were generated in CrystalMaker ® v8.7.6.

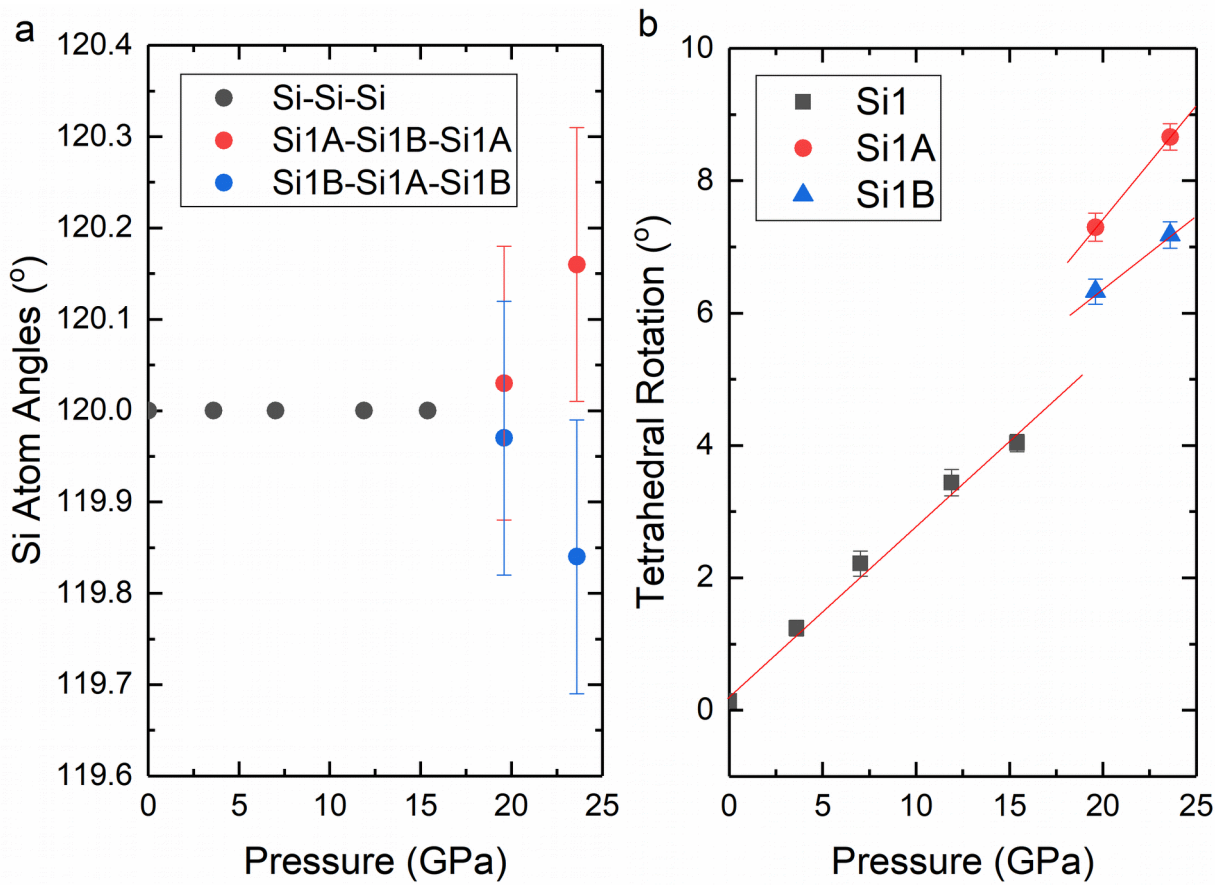

Figure 11. (a) Si-Si-Si atom angles and (b) tetrahedral rotation as a function of pressure. Note that the errors on bond angles are typically quite large; however, by ~23.6 GPa the deviation away from 120° is larger than the errors. The discontinuous shift in tetrahedral rotation near 15.4 GPa shows that the phase transition occurs near this pressure, but the pressure dependence of rotation is only slight altered in the high-pressure phase.

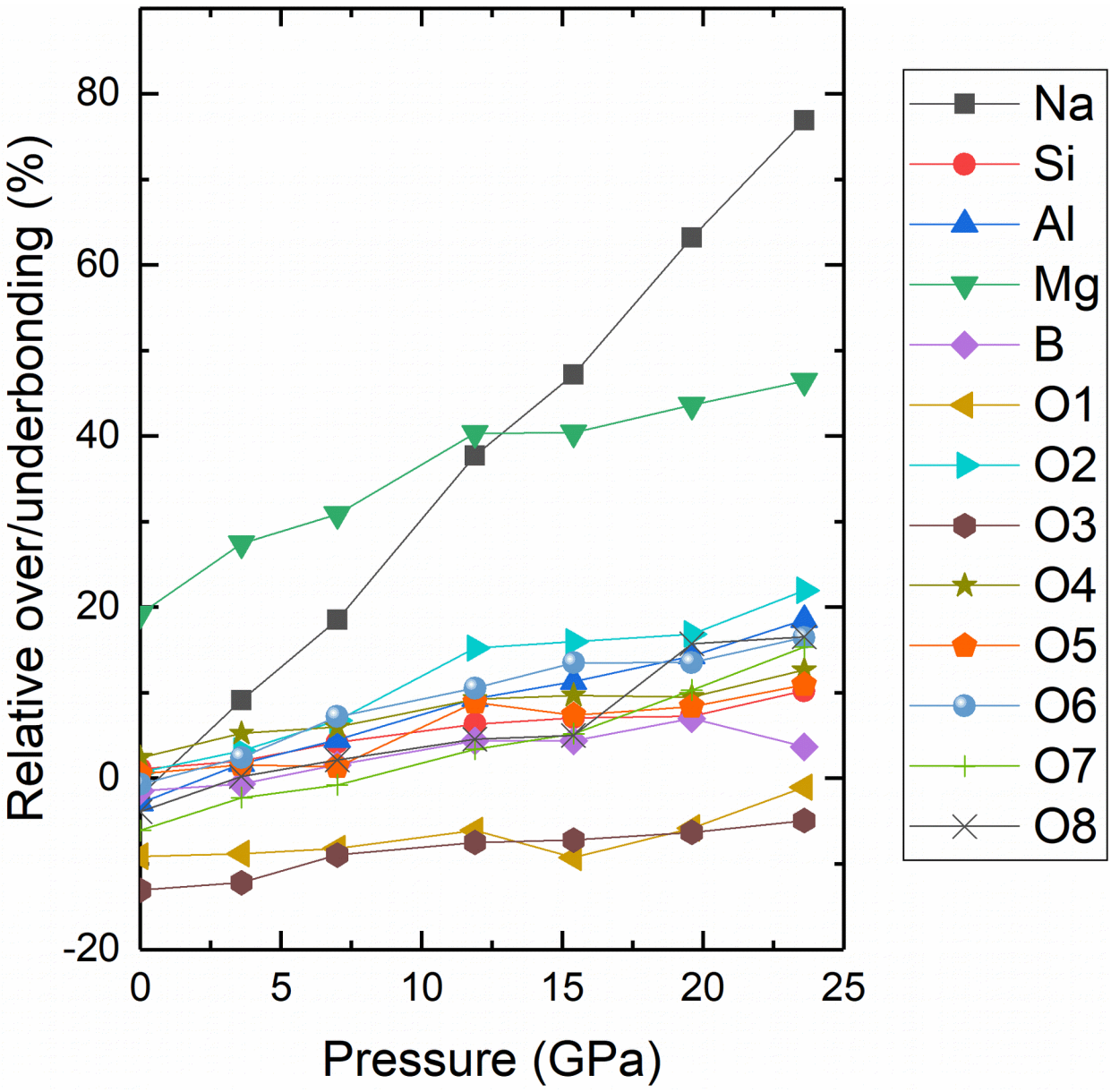

Figure 12. Bond valence calculations for different ions within the dravite tourmaline structure as a function of pressure.

Pressure (GPa)	*a*-axis (Å)	*c*-axis (Å)	Volume (Å^3)
*0.0001	15.9370(6)	7.1749(4)	1578.19(14)
1.4(1)	15.8820(8)	7.1258(4)	1556.60(22)
*3.6(2)	15.8180(7)	7.0534(3)	1528.38(22)
5.0(1)	15.7860(7)	7.0198(3)	1514.95(20)
*7.0(1)	15.7323(7)	6.9617(4)	1492.20(20)
7.1(1)	15.7219(8)	6.9628(4)	1491.83(22)
8.3(2)	15.7015(8)	6.9344(4)	1480.55(23)
9.4(2)	15.6711(7)	6.9066(4)	1468.91(21)
10.6(2)	15.6418(10)	6.8794(5)	1457.66(29)
*11.9(2)	15.6040(4)	6.8401(17)	1442.30(70)
13.2(3)	15.5765(14)	6.8127(7)	1431.53(40)
*15.4(4)	15.5214(21)	6.7796(11)	1414.48(58)
*19.6(4)	15.4491(13)	6.6948(6)	1383.80(32)
*23.6(5)	15.3537(15)	6.6419(6)	1355.97(37)

Table 1. Unit cell parameters of dravite tourmaline at various pressures. *Crystal structures solved at these pressures

Sample	V_0 (Å^3)	K_0 (GPa)	K'_0 (GPa)	Method	Reference
Schorl	1595.52(1.98)	183.5(4.2)	4(fixed)	Powder XRD	Li et al. (2004)
Uvite	1537.1(11)	96.6(9)	12.5(4)	Powder XRD	Xu et al. (2016)
		120(2)	4(fixed)	Powder XRD	Xu et al. (2016)
Dravite	1578.19(14)	109.0(2.9)	4.8(8)	Single crystal	This study
		112.2(9)	4(fixed)	Single crystal	This study

Table 2. Pressure-volume data fit up to ~15.4 GPa using both 2nd and 3rd order Birch-Murnaghan equations of state.

Pressure (GPa)	0.0001	3.6(2)	7.0(1)	11.9(2)	15.4(4)
Temperature (K)	298(2)	298(2)	298(2)	298(2)	298(2)
Crystal System, space group	rhombohedral *R3m*	rhombohedral *R3m*	rhombohedral *R3m*	rhombohedral *R3m*	rhombohedral *R3m*
a (Å)	15.9370(6)	15.8180(7)	15.7323(7)	15.6040(4)	15.5214(21)
c (Å)	7.1749(3)	7.0534(3)	6.9617(4)	6.8401(17)	6.7796(11)
Volume (Å^3)	1578.19(14)	1528.38(22)	1492.20(20)	1442.30(70)	1414.48(58)
R_1 (%)	2.99	6.57	4.89	4.07	3.07
wR_2 (%)	7.35	16.23	11.86	9.83	8.33
Goodness-of-fit	1.079	1.158	1.238	1.267	1.193
No. refined parameters	44	44	44	44	44

19.6(4)	23.6(5)
298(2)	298(2)
rhombohedral	rhombohedral
R3	*R3*
15.4491(13)	15.3537(15)
6.6948(6)	6.6419(6)
1383.80(32)	1355.97(37)
6.95	7.35
17.60	18.50
1.050	1.056
70	70

Table 3. Crystal structure refinement details for dravite tourmaline at various pressures. Complete CIFs can be found in the supplementary material.